Magnetoelasticity and *H-T* phase diagram of $TbNi_2B_2C$

M. ElMassalami
Instituto de Fisica, Universidade Federal do Rio de Janeiro, Caixa Postal 68528, 21945-970 Rio de Janeiro, Brazil

M. Amara and R.-M. Galéra
Institut Néel-CNRS, Bâtiment D, Boîte Postale 166, 38042 Grenoble Cedex 9, France

D. Schmitt
LGIT, 1381 Rue de la Piscine, Domaine Universitaire, 38400 Saint-Martien d'Hères, France

H. Takeya
National Institute for Materials Science, 1-2-1 Sengen, Tsukuba, Ibaraki 305-0047, Japan
(Received 2 June 2007; published 10 September 2007)

We investigated the magnetoelastic and magnetic properties of single-crystal $TbNi_2B_2C$ within the paramagnetic and ordered phases and along both *a* and *c* axes. The measured paramagnetic and gamma-parastriction susceptibilities are satisfactorily reproduced by the theoretical calculations based on crystalline electric field and molecular field approximations. The features of the γ-symmetry lowering mode indicate a noticeable orthorhombic distortion within both paramagnetic and magnetically ordered regions. The *H-T* phase diagram ($H\|a$) reveals a cascade of transformations that delineate the phase boundaries between a weak-ferromagnetic (WF) phase, an intermediate phase, and a paramagnetic saturated state. Interestingly, below 9 K and within the low-field regime, the phase boundary enclosing the WF state shows a reentrant behavior. Such a reentrance feature is associated with the presence of the net ferromagnetic component below T_{WF}.

DOI: 10.1103/PhysRevB.76.104410 PACS number(s): 75.20.En, 75.80.+q, 75.30.Kz

I. INTRODUCTION

Magnetoelastic interactions in rare-earth-based intermetallic compounds are, in general, associated with two contributions:[1] (i) a two-ion term related to the strain modulation of the exchange interactions and (ii) a single-ion term reflecting the strain modulation of the crystalline electric field (CEF) energy. Both contributions are evident in the tetragonal ($I4/mmm$) borocarbide series RNi_2B_2C: The two-ion effect is evident in the $^{7/2}S$-state $GdNi_2B_2C$ (Refs. 2–4), while the single-ion effect is predominant in compounds with, e.g., R=Tb,[5–8] Dy,[9,10] Ho,[11,12] and Er.[13–15]

Compared to other terms in the magnetic Hamiltonian of borocarbides, these magnetoelastic interactions are not negligible; in fact, their presence is manifested in various properties; the most prominent example is the spontaneous tetragonal-to-orthorhombic distortion observed in compounds with R=Tb,[5–8] Dy,[10] Ho,[11,12] and Er.[13–15] Then, it is of interest to extensively investigate the character and strength of these interactions across the borocarbide series. Toward this objective, the present work reports the characterization of magnetoelastic interactions in $TbNi_2B_2C$. This compound is strongly anisotropic[16,17] and orders magnetically, at T_N=15 K, into a longitudinal, sinusoidal wave, $q=(0.55,0,0)$, with the moments pointing along the *a* axis.[18–20] Concomitant with this transition, the above-mentioned orthorhombic distortion sets in.[5,6,8] As the temperature is lowered further, there is a progressive increase in the intensity of higher order harmonic modes and, at T_{WF}=8 K, the modulation squares up and locks in to a commensurate state which is accompanied, as a by-product,[21,22] by a surge of a weak ferromagnetic component.

Here, we report single-crystal magnetostriction and magnetization measurements over wide ranges of temperatures and fields. Within the paramagnetic phase, an appreciable field-induced orthorhombic distortion is observed; this is taken to be indicative of a sizable γ-symmetry magnetoelastic coupling. That such an orthorhombic distortion is operative within the magnetically ordered phase can be observed in the features of the low-temperature magnetic phase diagram with $H\|a$ axis. In this *H-T* diagram, various phase boundaries are observed and identified. In particular, the boundary enclosing the weak-ferromagnetic state is followed over a considerable span of fields and temperatures. Interestingly, within certain ranges of fields and temperatures, a reentrant behavior of this weak-ferromagnetic (WF) state is manifested.

II. EXPERIMENT

$TbNi_2B_2C$ single crystals were grown by the floating zone method.[23] The measurements were carried out on annealed rectangular bars; different bars are cut along different crystallographic directions. Such a parallelepiped geometry ($\sim 1\times 1\times 10$ mm^3) gives rise to demagnetizing effects, the strength of which depends on the alignment of the parallelepiped relative to the applied magnetic field.

The (isofield and isothermal) magnetization curves were measured on an extraction-type magnetometer (1.5 K$\leqslant T\leqslant$300 K, $H\leqslant$110 kOe) with a sensitivity around 5×10^{-4} emu. The paramagnetic susceptibilities (25 K$\leqslant T\leqslant$300 K) were deduced from isothermal Arrott plots (M^2 versus H/M).

A high-accuracy capacitance dilatometer was used for measuring the thermal expansion or forced magnetostriction (3 K$\leqslant T\leqslant$250 K, $H\leqslant$65 kOe) with a resolution better than

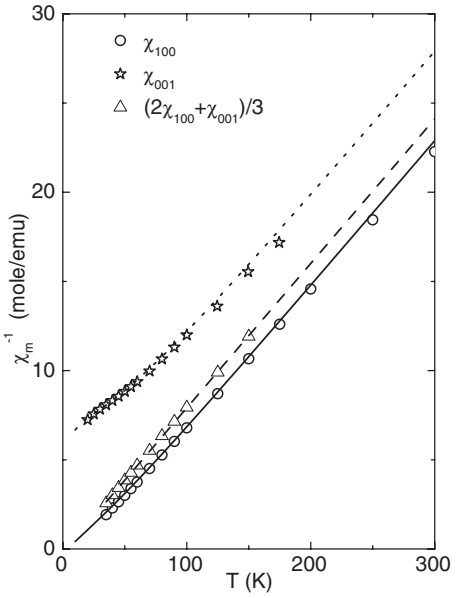

FIG. 1. Thermal variation of the reciprocal paramagnetic susceptibilities [χ_{100}^{-1}, χ_{001}^{-1}, and the powder average $3/(2\chi_{100}+\chi_{001})$] of $TbNi_2B_2C$. The lines represent the calculated curves based on the crystal field and molecular field formalism using n and CEF parameters as given in the text.

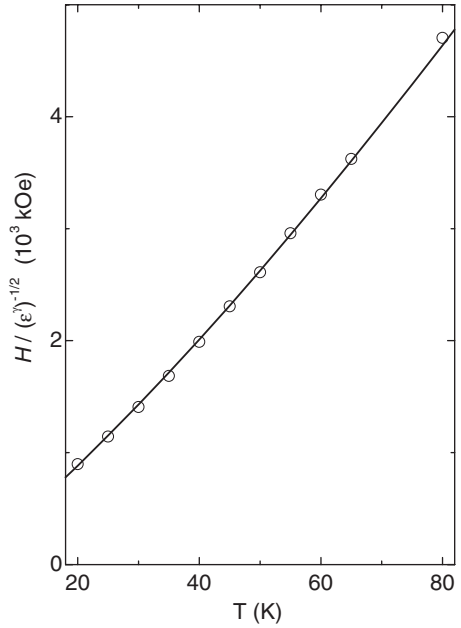

FIG. 2. Thermal variation of $H/\sqrt{\epsilon^{\gamma}}$ for H along the (100) direction (for definitions see the Appendix). The line represents the calculated curve (see text).

1 Å. In this setup, the applied field is along a fixed horizontal direction, while the capacitance cell—together with the sample—can be rotated around the vertical axis. With this arrangement, the angle ϕ between the field cosine direction (xyz) and the probed strain-variation cosine direction $(\beta_1\beta_2\beta_3)$ can be varied over a range of 180°: Both axes of the field and the probed length change are horizontal. The relative change in length measured along $(\beta_1\beta_2\beta_3)$ when a field is applied along (xyz) is denoted as ${}^{\beta_1\beta_2\beta_3}\lambda_{xyz}(T) = [l(T,H) - l_0(T_0,H_0)]/l_0(T_0,H_0)$. For a temperature (field) scan, H (T) is fixed and l_0 is taken as the length at the reference T_0 (H_0).

We carried out extensive measurements of ϕ-, H-, and T-dependent strains ${}^{\beta_1\beta_2\beta_3}\lambda_{xyz}$: For H and T scans, the directions (xyz) and $(\beta_1\beta_2\beta_3)$ are limited to the principal axes (100), (010), and (001). This allowed us, particularly within the paramagnetic phase, to investigate separately each of the normalized, symmetrized strains $\epsilon^{\alpha 1}$, $\epsilon^{\alpha 2}$, and ϵ^{γ} (see the Appendix). The H-T phase diagram for $H\|a$ has been constructed based on the overall analysis of the events occurring in the low-temperature magnetization and magnetostriction curves.

III. RESULTS AND DISCUSSION

A. Paramagnetic phase

The paramagnetic susceptibilities (Fig. 1) along both a and c axes (χ_{100} and χ_{001}, respectively) follow a Curie-Weiss law at high temperatures. The effective magnetic moment deduced from the slope of the averaged curve is $9.9\mu_B$, which is only 2% higher than the theoretical value of the free Tb^{3+} ion ($9.72\mu_B$). The experimental susceptibilities are satisfactorily reproduced by theoretical calculation based on CEF and molecular field approximations if one takes the molecular field constant as $n=0.15$ mole/emu ($\theta_p=3.2$ K), the quadrupolar parameters as $G_{\alpha}=0$, $G_{\gamma}=15\times10^{-4}$, and $G_{\epsilon}=0$, and the crystal field parameters as $B_2^0=1.2$ K, $B_4^0=41\times10^{-4}$ K, $B_4^4=-0.065$ K, $B_6^0=-36\times10^{-6}$ K, and $B_6^4=-1\times10^{-4}$ K.

Figure 2 shows the thermal evolution of $H/\sqrt{\varepsilon^{\gamma}}$ versus T for $H\|a$ confirming[5–8] that, even within the paramagnetic phase, a sizeable orthorhombic distortion is being induced: Thus, the magnitude of the quadrupolar susceptibility associated with the symmetry lowering mode is relatively strong. The $H/\sqrt{\varepsilon^{\gamma}}$ curves in Fig. 2 were constructed from parastriction curves according to the formulas collected in the Appendix. Using similar procedures, we obtained $H/\sqrt{\varepsilon^{\alpha_1}(T)}$ and $H/\sqrt{\varepsilon^{\alpha_2}(T)}$ curves (not shown). The strength of ε^{α_1} and ε^{α_2} are observed to be smaller than ϵ^{γ}; nevertheless, they indicate a noticeable volume and axial distortions when $H\|a$. In contrast, we observed only a very small volume and axial distortion when the field is applied along $H\|c$. Both observations are consistent with the sign of the B_2^0 parameter, which favors the easy direction to be perpendicular to the c axis.

Using CEF and molecular field approximations, we calculated χ_{100}, χ_{001}, and the symmetrized strain ϵ^{γ}. Our calculations are based on taking B_2^0 and θ_p as being experimentally-determined while the values of B_4^0, B_4^4, B_6^0, and B_6^4 as well as the B^{μ} and C^{μ} coefficients are to be adjusted so that the experimental curves are reproduced. A reasonable agreement between the calculated and measured curves of $H/\sqrt{\varepsilon^{\gamma}(T)}$ as well as $\chi_{100}^{-1}(T)$ and $\chi_{001}^{-1}(T)$ (see Figs. 1 and 2) is reached when the above-mentioned parameters are used. It is worth-

while mentioning that the same set of CEF and molecular field parameters are less successful in reproducing the experimental curves of $H/\sqrt{\varepsilon^{\alpha 1}(T)}$ and $H/\sqrt{\varepsilon^{\alpha 2}(T)}$ possibly due to large experimental errors stemming from the relatively weaker parastriction values. Nevertheless, it is assuring that a rough approximation gives $A^{\alpha 1} \approx 2.5 \times 10^{-5}$, $A^{\alpha 2} \approx 10 \times 10^{-5}$, and $\frac{B^{\gamma}}{C_0^{\gamma}} \approx 9 \times 10^{-5}$. In particular, $\frac{B^{\gamma}}{C_0^{\gamma}}$ compares favorably well with the expected value of $\approx 10^{-4}$ for the typical case wherein $B^{\gamma} \approx 10$ K and $C^{\gamma} \approx 10^5$ K/atom.[1]

It is needless to mention that the determination of such large numbers of parameters based only on the measured magnetic (Fig. 1) and quadrupolar (Fig. 2) susceptibilities would not provide a unique set of values and, therefore, except for the determination of θ_p, B_2^0, and G_{γ}, these determined values should be taken as indicative. It is noted that the available sets of CEF parameters are in disarray and are different from the parameters determined in this work: As an example, the CEF parameters estimated, through extrapolation arguments, by Gasser *et al.*[24,25] ($B_2^0 = 1.81$ K, $B_4^0 = 0.004\,11$ K, $B_4^4 = -0.1199$ K, $B_6^0 = 2.5 \times 10^{-5}$ K, and $B_6^4 = -2.94 \times 10^{-4}$ K) are different from the ones obtained, through a fit to inelastic neutron scattering curves, by Rotter *et al.*[26] ($B_2^0 = 1.65$ K, $B_4^0 = 0.007\,06$ K, $B_4^4 = -7.86 \times 10^{-4}$ K, $B_6^0 = -5.02 \times 10^{-5}$ K, and $B_6^4 = -1.22 \times 10^{-4}$ K). In fact, there is a disagreement even in the value of B_2^0: Neither the value obtained in this work nor the ones reported in Refs. 24–26 agree with the one reported by Cho *et al.* [16] ($B_2^0 = 1.5$ K). Such a discrepancy highlights the need for further studies on the CEF properties.

B. Ordered phase

1. Magnetization

The $M(H\|a)$ isotherms [see Fig. 3(a)] demonstrate, in agreement with earlier observations,[16,17] a series of magnetic transitions occurring at H_{WF} (associated with the WF state), H_2, and H_S (the saturated paramagnetic state). At lower fields, there is, in addition, the domain-wall motion; its sweeping-out field is denoted as H_D. These events are most visible in the field-derivative curves (not shown) and in the isothermal magnetostriction curves (see below). Based on these events as well as on those appearing in the $M(T)$ isofield curves (not shown), the magnetic phase diagram ($H\|a$) is constructed (see below). As the c axis is the hard direction, no transitions for the case of $H\|c$ [other than the one at $T_N(H)$] are observed within our range of fields and temperatures.

Magnetic phase transitions, such as the ones shown in Fig. 3, are not uncommon in borocarbides[27] and are generally interpreted in terms of a magnetic Hamiltonian that consists basically of the Ruderman-Kittel-Kasuya-Yosida-type exchange couplings, the Zeeman term, and the CEF interactions.[28,29] Additionally, magnetoelastic or dipolar interactions are also considered.[3,15,22] In line with this scenario, the magnetic transitions of $TbNi_2B_2C$ are envisaged as being due to a balance between these (competing) interactions.

2. Magnetostriction

Figure 3(b) shows the forced magnetostriction isotherms measured along (100) with $H\|a$. Once more, the transitions

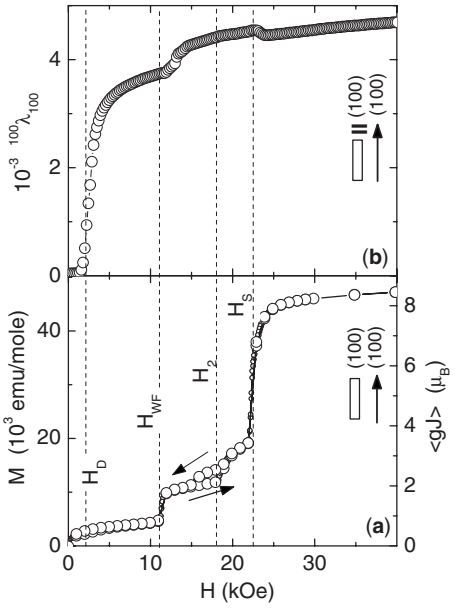

FIG. 3. Field-dependent isotherms of the magnetization [panel (a)] and magnetostriction [panel (b)] of $TbNi_2B_2C$ ($H\|a$, 3 K). Samples are represented by small rectangles, H directions by vertical arrows, and the capacitor plates by two thick, short parallel lines. λ is measured parallel to the long side of the rectangle.

at H_{WF}, H_2, and H_S are clearly visible and more so in the field-derivative curves. A close look at $M(H\|a)$ [Fig. 3(a)] and $^{100}\lambda_{100}(H)$ [Fig. 3(b)] curves reveals that while the length variation in the magnetostriction curve attains its almost full value at H_D, the magnetization saturation is reached only at H_S. This is in line with the fact that the low-temperature ordered state is a uniaxial squared-up modulated state:[21,22] Considering that initially there is an equal distribution of domains along each of the a and b axes, then an applied $H(\|a)$ would initially favor the domain alignment along the a axis, leading to a huge magnetostriction effect but resulting in only a weak moment of the order of $0.5\mu_B$ (the WF component). On a further progressive increase of the applied field, $M(H\|a)$ (being proportional to the magnetic moment vector) would reflect each of the transitions at H_{WF}, H_2, and H_S, while the forced single-ion magnetostriction (being proportional to the square of the moment vector) would hardly show any of these events occurring at such critical fields. Then, those weaker transitions observed in the magnetostriction curves at H_{WF}, H_2, and H_S must be due to the weaker two-ion effect. This statement is supported by Fig. 4, which shows the forced magnetostriction isotherms along the b and c axes, all under $H\|a$. A comparison of the field evolution of $^{010}\lambda_{100}(H)$ and $^{001}\lambda_{100}(H)$ shows that the relative variations along the hard c axis is an order of magnitude weaker (since predominantly two-ion effect) than that along the basal plane (predominantly due to domain-wall motion). It is worthwhile mentioning that the domain-wall motion within the basal plane involves a considerable spacial rearrangement of the orthorhombically distorted domains. During this rearrangement, $^{100}\lambda_{100}(H)$ increases while $^{010}\lambda_{100}(H)$ decreases (see Fig. 5).

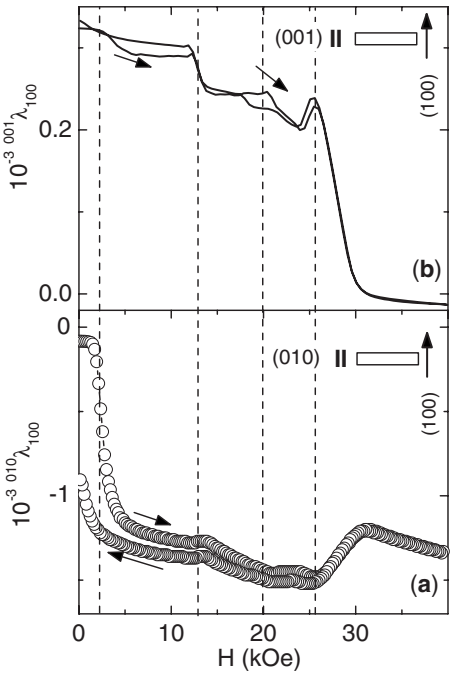

FIG. 4. Forced magnetostriction isotherms of $TbNi_2B_2C$ measured at 3 K for increasing and decreasing fields [(a) $^{010}\lambda_{100}(H)$; (b) $^{001}\lambda_{100}(H)$]. Samples are represented by small rectangles, the fields ($H \| a$) by vertical upward arrows, and the capacitor plates by two thick, short parallel lines. λ is measured parallel to the long side of the sample.

It is noticeable that the transformations in $^{100}\lambda_{100}(H)$ [Fig. 3(b)], $^{010}\lambda_{100}(H)$ [Fig. 4(a)], and $^{001}\lambda_{100}(H)$ [Fig. 4(b)] are not manifested at the same field values. Since the demagnetizing field is much lower (larger) when the longer side of the rectangular sample is parallel (perpendicular) to the applied field, then a transition at H_S for example, is manifested at a higher applied field in $^{010}\lambda_{100}(H)$ or $^{001}\lambda_{100}(H)$ than in $^{100}\lambda_{100}(H)$ (see Figs. 3 and 4). Below, for compatibility purposes, only the transitions obtained from $M_{100}(H)$ and $^{100}\lambda_{100}(H)$ are used for the construction of the phase diagram.

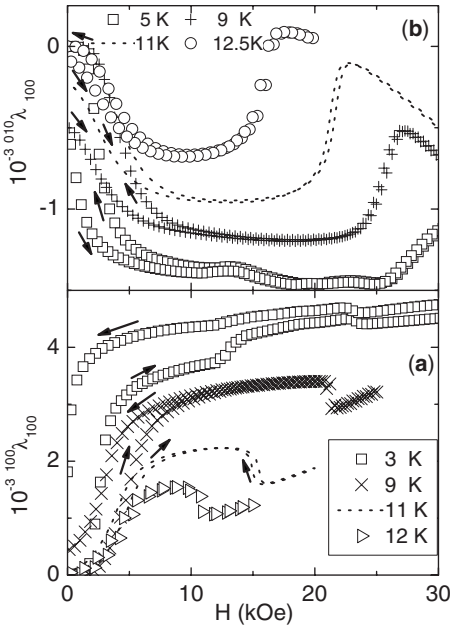

FIG. 5. Forced magnetostrictions [(a) $^{100}\lambda_{100}(H)$; (b) $^{010}\lambda_{100}(H)$] of $TbNi_2B_2C$ for increasing and decreasing fields taken at various fixed temperatures.

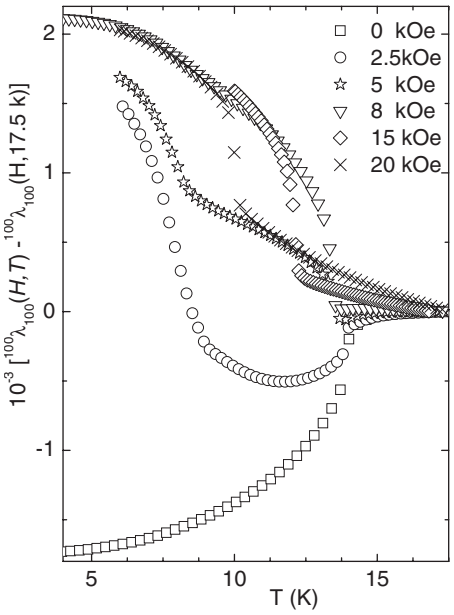

FIG. 6. Representative $^{100}\lambda_{100}(T)$ curves of $TbNi_2B_2C$ taken at various fixed fields. All curves are given relative to their values at 17.5 K.

Additional $^{100}\lambda_{100}(H)$ and $^{010}\lambda_{100}(H)$ isotherms are shown in Fig. 5. Evidently, while the events at H_D and H_S are visible for all $T < T_N$, the intensity of the transformations at H_2 diminishes as $T \rightarrow T_{WF}$ and disappears altogether for $T \geqslant T_{WF}$. These findings are evident also in the reported $M_{110}(H)$ isotherm.[16]

Figure 6 shows the thermal evolution of $^{100}\lambda_{100}(T)$ for different fixed fields; once more, the same series of transitions can be easily identified. Interestingly, the zero-field $^{100}\lambda_{100}(T)$ curve in Fig. 6 does not manifest any anomaly at T_{WF}, though the zero-field ac susceptibility[17] and specific heat[30] do manifest that anomaly: Considering that there are no anomalous thermal expansion behavior, this feature is attributed to the fact that under zero field the domains are distributed equally among the allowed easy *a* and *b* axes.

The angular scans of Fig. 7 demonstrate the process of domain switching between two states, one with moments aligned along the *a* axis and another along the *b* direction: This gives an additional support to the above-mentioned arguments concerning the magnetostriction and magnetization of the orthorhombically distorted, uniaxial squared-up state. Moreover, the difference curve $[^{100}\lambda(0°) - {}^{100}\lambda(90°)]$ has a much higher resolution, but is in agreement with the mismatch parameter $(a/b-1)$ reported in Ref. 5. Such an agreement is demonstrated as well in Fig. 8 wherein the thermal evolution of the field-induced orthorhombic distortion, ϵ^{γ}, is shown: In fact, the curve at $H=5.0$ kOe is a good approximation of the spontaneous magnetostriction.

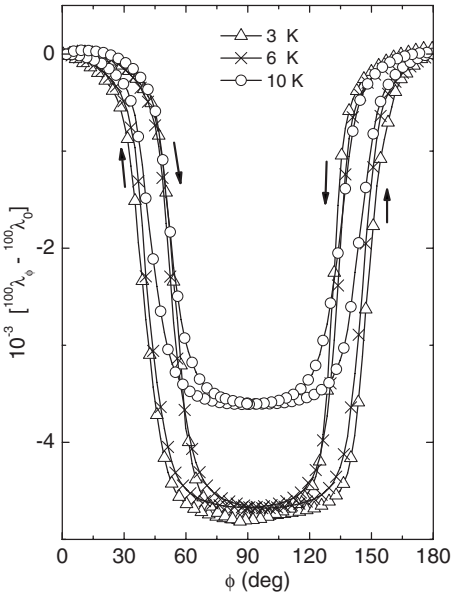

FIG. 7. Angular dependence of $^{100}\lambda_\phi$ isotherms under $H=8$ kOe and for $T=3$, 6, and 10 K. The zero reference is taken as the value of $^{100}\lambda(\phi=0)$.

3. Phase diagram

The magnetic phase diagram for $H\|a$ (Fig. 9) reveals the thermal evolution of the phase boundaries $H_{WF}(T)$, $H_2(T)$, and $H_S(T)$. As mentioned above, $H_{WF}(T)$, $H_2(T)$, and $H_S(T)$ are related, respectively, to the WF event, the second metamagnetic transformation, and the moment saturation process. Interestingly, $H_{WF}(T)$ shows a reentrant behavior at and around T_{WF}: This is associated with the fact that for temperatures immediately above $T_{WF}(H=0)$, it is energetically more favorable to assume a state wherein a ferromagnetic component appears (thus gaining an additional Zeeman energy). As a consequence, the $H_{WF}(T)$ curve should preferably cross the temperature axis with a smaller positive tangent (in fact, thermodynamical arguments suggest that if this is a transition, then the tangent should be horizontal). For higher fields, $H_{WF}(T)$ develops a concave curvature and tends toward saturation (12 kOe) at lower temperatures. These features are evident also in, e.g., $ErNi_2B_2C$ (Ref. 15) and should be typical for any magnetic state with a similar WF component.

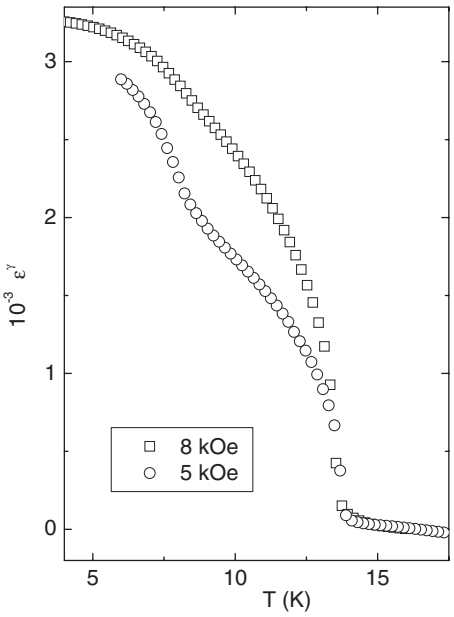

FIG. 8. Thermal evolution of ϵ^γ taken at $H=5.0$ and 8 kOe.

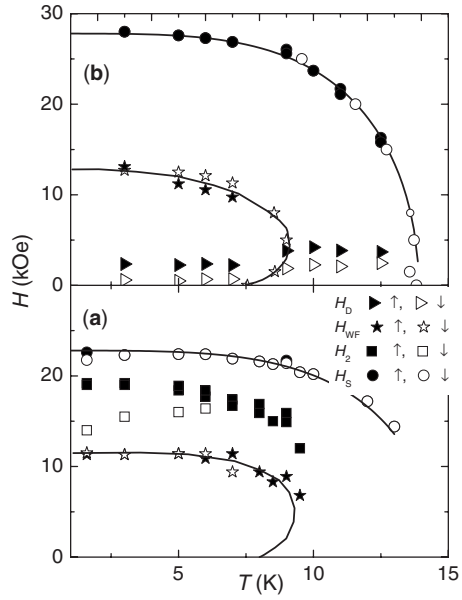

FIG. 9. The *H-T* phase diagram of $TbNi_2B_2C$ ($H\|a$) as compiled from the (a) magnetization and (b) magnetostriction measurements. Since the transitions are revealed differently by each technique (see text), these two panels are complementary. The continuous lines are guides to the eye. Filled (unfilled) symbols represent measurements during an increasing (decreasing) field sweep. Phase boundary identifications are given in the text. Note that while H_D and H_2 show hysteresis effects, H_S and H_{WF} do not. The anomalous temperature dependence of H_D is emphasized in both panels.

The presence of the WF state with its characteristic reentrant $H_{WF}(T)$ curve hinders the easy elucidation of how $H_2(T)$ evolves within the temperature range neighboring or immediately above $T_{WF}(H=0)$; nevertheless, this WF presence renders the field-induced motion of the domain walls much easier: This explains the anomalous temperature dependence of $H_D(T)$ observed in Fig. 9 wherein $H_D(T>T_{WF})$ is higher than $H_D(T<T_{WF})$.

Notable hysteresis effects are observed only at H_D and H_2 processes. While the hysteresis in H_D is typical for domain processes, its origin in H_2 is not clear. Assuming that the transition at H_2 is due to a change in the value of the modulation vector, then this phase transition is most probably of a first-order type. Furthermore, on a closer look at Fig. 3(a), one observes a clear structure of this H_2 transition, possibly due to two different unresolved transitions or an admixture of the two neighboring phases. The identification of two branches in H_2 is better revealed in the field-decrease cycle and even more apparent on considering the field derivative of

the magnetization. The thermal evolution of these two branches is shown in Fig. 9: As $T \rightarrow T_{WF}$, both branches merge into the H_2 boundary. On the other hand, as $T \rightarrow 0$ K, the upper branch saturates to 19.3 kOe while the lower one seemingly tends to merge with the WF phase boundary.

Finally, the magnetic phase diagram for $H \| (110)$, extensively studied by Cho *et al.*,[16] shows only the hysteresisless $H_{WF}(T)$ boundary and the $H_S(T)$ curve (see Fig. 6 of Ref. 16). It is not clear whether $H_2(T)$, with its characteristic hysteresis, is absent altogether or merges into either $H_{WF}(T)$ or $H_S(T)$.

IV. CONCLUSIONS

Magnetoelastic phenomena in $TbNi_2B_2C$ were studied within both the paramagnetic and ordered phases. Within the paramagnetic state, the measured parastriction and magnetic susceptibilities are compared with theoretical calculation based on CEF and molecular field approximations. These studies reveal the presence of a noticeable field-induced orthorhombic distortion (ϵ^{γ}) within the paramagnetic phase. On the other hand, the *H-T* phase diagrams, reported for $H \| a$, reveal a cascade of (four) magnetic events, which are identified as follows: (i) The event at $H_D(T)$ is associated with the domain-wall motion. H_D is observed to be weaker within the WF phase than above T_{WF}. This is so because it is much easier to rotate an orthorhombic domain wherein there is a net ferromagnetic component than otherwise. (ii) The phase boundary at $H_{WF}(T)$ is related to the WF state. Interestingly, this boundary line indicates a reentrant feature in the neighborhood of $T_{WF}(H=0)$. Such reentrance is attributed to the fact that within this range of field and temperature, an applied field favors a WF state since the system gains an additional Zeeman energy. (iii) The transformation at $H_2(T)$ is related to a metamagnetic transition involving, presumably, a change in the modulation vector. At this transition, two shoulders are evident in the isothermal magnetization curves when $T < T_{WF}$. Finally, (iv) the $H_S(T)$ phase boundary is related to the saturation process.

ACKNOWLEDGMENTS

We acknowledge the partial financial support from the Brazilian agencies CNPq (485058/2006-5) and Faperj (E-26/171.343/2005).

APPENDIX: ANALYTICAL EXPRESSIONS FOR THE PARASTRICTION SUSCEPTIBILITIES (REFERENCE 1)

For the purpose of calculating the paramagnetic and parastriction susceptibilities of tetragonal $TbNi_2B_2C$, we assume the following Hamiltonian (considering the magnetoelasticity to be due only to a one-ion effect):

$$\mathcal{H}_{tot} = \mathcal{H}_{CEF} + \mathcal{H}_Z + \mathcal{H}_{ex} + \mathcal{H}_Q, \tag{A1}$$

which consists, respectively, of the crystal field, Zeeman, exchange, and total quadrupolar interactions. In this case, the CEF term is

$$\mathcal{H}_{CEF} = B_2^0 O_2^0 + B_4^0 O_4^0 + B_4^4 O_4^4 + B_6^0 O_6^0 + B_6^4 O_6^4, \tag{A2}$$

while the Zeeman part is

$$\mathcal{H}_Z = g_J \mu_B J H$$

and the exchange term is:

$$\mathcal{H}_{ex} = -n(g_J \mu_B)^2 \langle J \rangle J,$$

where n is the usual isotropic bilinear coupling constant related to the paramagnetic temperature as $n = 3k_B\theta_p/(g_J\mu_B)^2 J(J+1)$. In the present calculation, the anisotropic bilinear coupling is neglected since it is relatively small compared to the stronger anisotropy originating from the CEF interactions. Indeed, for $TbNi_2B_2C$, $n \approx -1$ mol/emu while in the isomorphous $GdNi_2B_2C$ compound, the anisotropic coupling constant is of the order of -0.05 mol/emu.[3] $\mathcal{H}_Q$ is given as

$$\mathcal{H}_Q = -G_2^{\alpha}\langle O_2^0 \rangle O_2^0 - G^{\gamma}\langle O_2^2 \rangle O_2^2 - G^{\delta}\langle P_{xy} \rangle P_{xy} - G^{\varepsilon}[\langle P_{yz} \rangle P_{yz} + \langle P_{zx} \rangle P_{zx}], \tag{A3}$$

where the G^{μ} are the total quadrupole couplings which, in turn, depend on the pair quadrupolar couplings K^{μ}, the elastic constants C_0^{μ}, and the magnetoelastic coefficients B^{μ}.

The first-order magnetic susceptibility is $\chi_M = \chi_0/(1 - n\chi_0)$, where χ_0 is the CEF susceptibility. The relative length change $\frac{\partial l}{l}$ measured along $(\beta_1, \beta_2, \beta_3)$ when $H \| (x, y, z)$ is expressed as

$$\beta_1\beta_2\beta_3\left(\frac{\partial l}{l}\right)_{xyz} = {}^{\beta_1\beta_2\beta_3}\lambda_{xyz} = \frac{1}{\sqrt{3}}\epsilon^{\alpha_1} + \frac{1}{\sqrt{6}}\epsilon^{\alpha_2}(2\beta_3^2 - \beta_1^2 - \beta_2^2) + \frac{1}{\sqrt{2}}\epsilon^{\gamma}(\beta_1^2 - \beta_2^2). \tag{A4}$$

Here, the only operative modes are assumed to be the volume, axial, and orthorhombic distortions, which are defined, respectively, as [taking the field along (100)]

$$\epsilon^{\alpha_1} = \frac{1}{\sqrt{3}}({}^{100}\lambda_{100} + {}^{010}\lambda_{100} + {}^{001}\lambda_{100}),$$

$$\epsilon^{\alpha 2} = \frac{1}{\sqrt{6}}(2 \cdot {}^{001}\lambda_{100} - {}^{100}\lambda_{100} - {}^{010}\lambda_{100}),$$

$$\epsilon^{\gamma} = \frac{1}{\sqrt{2}}({}^{100}\lambda_{100} - {}^{010}\lambda_{100}). \tag{A5}$$

Similarly, when the field is applied along (001), we get

$$\epsilon^{\alpha_1} = \frac{1}{\sqrt{3}}(2 \cdot {}^{100}\lambda_{001} + {}^{001}\lambda_{001}),$$

$$\epsilon^{\alpha 2} = \frac{2}{\sqrt{6}}({}^{001}\lambda_{001} - {}^{100}\lambda_{001}). \tag{A6}$$

At equilibrium, the symmetrized strains (disregarding the weak two-ion effect) are given by

$$\epsilon^{\alpha 1} = \frac{B^{\alpha 1} C_0^{\alpha 2} - B^{\alpha 2} C_0^{\alpha 12}}{C_0^{\alpha 1} C_0^{\alpha 2} - (C_0^{\alpha 12})^2} \langle O_2^0 \rangle = A^{\alpha 1} \langle O_2^0 \rangle = A^{\alpha 1} \chi_Q^{\alpha 1} H^2, \quad \text{(A7)}$$

$$\epsilon^{\alpha 2} = \frac{B^{\alpha 2} C_0^{\alpha 1} - B^{\alpha 1} C_0^{\alpha 12}}{C_0^{\alpha 1} C_0^{\alpha 2} - (C_0^{\alpha 12})^2} \langle O_2^0 \rangle = A^{\alpha 2} \langle O_2^0 \rangle = A^{\alpha 2} \chi_Q^{\alpha 2} H^2, \quad \text{(A8)}$$

$$\epsilon^{\gamma} = \frac{B^{\gamma}}{C_0^{\gamma}} \langle O_2^2 \rangle = \chi_Q^{\gamma} H^2, \quad \text{(A9)}$$

where the B^{μ} are the magnetoelastic coefficients, while the C_0^{μ} are the symmetrized elastic constants. χ_Q^{μ} are the total quadrupole field susceptibilities, which are given by

$$\chi_Q^{\mu} = \frac{\chi_{\mu}^{(2)}}{(1 - n\chi_0)^2 (1 - G^{\mu} \chi_{\mu})},$$

where $\chi_{\mu}^{(2)}$ is the quadrupolar-field susceptibility, while χ_{μ} is the strain susceptibility.

[1] P. Morin and D. Schmitt, in *Ferromagnetic Materials*, edited by K. H. J. Buschow and E. P. Wohlfarth (Elsevier Science, Amsterdam, The Netherlands, 1990), pp. 1–132.

[2] P. C. Canfield, B. K. Cho, and D. C. Johnston, Physica B **215**, 337 (1995).

[3] M. E. Massalami, H. Takeya, K. Hirata, M. Amara, R.-M. Galera, and D. Schmitt, Phys. Rev. B **67**, 144421 (2003).

[4] M. Rotter, A. Lindbaum, A. Barcza, M. El Massalami, M. Doerr, M. Loewenhaupt, M. Michor, and B. Beuneu, Europhys. Lett. **75**, 160 (2006).

[5] C. Song, Z. Islam, L. Lottermoser, A. I. Goldman, P. C. Canfield, and C. Detlefs, Phys. Rev. B **60**, 6223 (1999).

[6] C. Song, D. Wermeille, A. I. Goldman, P. C. Canfield, J. Y. Rhee, and B. N. Harmon, Phys. Rev. B **63**, 104507 (2001).

[7] C. Song, J. C. Lang, C. Detlefs, A. Letoublon, W. Good, J. Kim, D. Wermeille, S. L. Bud'ko, P. C. Canfield, and A. I. Goldman, Phys. Rev. B **64**, 020403(R) (2001).

[8] C. Detlefs, C. Song, S. Brown, P. Thompson, A. Kreyssig, S. L. Budko, and P. C. Canfield, arXiv:cond-mat/0306742 (unpublished).

[9] Z. Q. Peng, K. Krug, and K. Winzer, Phys. Rev. B **57**, R8123 (1998).

[10] C. Sierks, M. Rotter, A. Kreyssig, M. Lowenhaupt, Z. Q. Peng, and K. Winzer, J. Magn. Magn. Mater. **192**, 473 (1999).

[11] G. Oomi, T. Kagayama, H. Mitamura, T. Goto, B. K. Cho, and P. C. Canfield, Physica B **294-295**, 229 (2001).

[12] A. Kreyssig, M. Loewenhaupt, J. Freudenberger, K. H. Muller, and C. Ritter, J. Appl. Phys. **85**, 6058 (1999).

[13] C. Detlefs, A. H. M. Z. Islam, T. Gu, A. I. Goldman, C. Stassis, P. C. Canfield, J. P. Hill, and T. Vogt, Phys. Rev. B **56**, 7843 (1997).

[14] A. Kreyssig, A. Schneidewind, M. Loewenhaupt, C. Ritter, J. Freudenberger, G. Fuchs, and K. H. Muller, Nato ARW Workshop, Dresden, 2000 (unpublished), Vol. 85.

[15] M. Doer, M. Rotter, M. El Massalami, S. Sinning, H. Takeya, and M. Loewenhaupt, J. Phys.: Condens. Matter **14**, 5609 (2002).

[16] B. K. Cho, P. C. Canfield, and D. C. Johnston, Phys. Rev. B **53**, 8499 (1996).

[17] C. V. Tomy, L. A. Afalfiz, M. R. Lees, J. M. Martin, D. M. Paul, and D. T. Adroja, Phys. Rev. B **53**, 307 (1996).

[18] P. Dervenagas, J. Zarestky, C. Stassis, A. I. Goldman, P. C. Canfield, and B. K. Cho, Phys. Rev. B **53**, 8506 (1996).

[19] A. Kreyssig, O. Stockert, A. Dreyhaupt, E. Ressouche, B. G. C. Ritter, H. Bitterlich, G. Behr, P. C. Canfield, and M. Loewenhaupt, J. Low Temp. Phys. **131**, 1129 (2003).

[20] J. W. Lynn, S. Skanthakumar, Q. Huang, S. K. Sinha, Z. Hossain, L. C. Gupta, R. Nagarajan, and C. Godart, Phys. Rev. B **55**, 6584 (1997).

[21] M. B. Walker and C. Detlefs, Phys. Rev. B **67**, 132407 (2003).

[22] J. Jensen, Phys. Rev. B **65**, 140514(R) (2002).

[23] H. Takeya, T. Hirano, and K. Kadowaki, Physica C **256**, 220 (1996).

[24] U. Gasser, P. Allenspach, J. Mesot, and A. Furrer, Physica C **282-287**, 1327 (1997).

[25] U. Gasser, P. Allenspach, F. Fauth, W. Henggeler, J. Mesot, A. Furrer, S. Rosenkranz, P. Vorderwisch, and M. Buchgeiste, Z. Phys. B: Condens. Matter **101**, 345 (1996).

[26] M. Rotter, C. Sierks, M. Loewenhaupt, J. Freudenberger, and H. Schober, in *Rare Earth Transition Metal Borocarbides (Nitrides): Superconducting, Magnetic and Normal State Properties*, Nato Advanced Research Workshop, edited by K. H. Müller and V. Narozhnyi (Kluwer Academic, Dordrecht, 2001), pp. 137–153.

[27] K.-H. Müller and V. N. Narozhnyi, Rep. Prog. Phys. **64**, 943 (2001).

[28] P. C. Canfield, S. L. Bud'ko, B. K. Cho, A. Lacerda, D. Farrell, E. Johnston-Halperin, V. A. Kalatsky, and V. L. Pokrovsky, Phys. Rev. B **55**, 970 (1997).

[29] A. Amici and P. Thalmeier, Phys. Rev. B **57**, 10 684 (1998).

[30] M. E. Massalami, R. E. Rapp, F. A. B. Chaves, H. Takeya, and C. M. Chaves, Phys. Rev. B **67**, 224407 (2003).